# 180° Rotations in the polarization angle for blazars

M. H. Cohen[1] and T. Savolainen[2, 3, 4]

[1] Department of Astronomy, California Institute of Technology, Pasadena, CA 91125, USA
 e-mail: mhc@astro.caltech.edu
[2] Aalto University Department of Electronics and Nanoengineering, PL 15500, FI-00076 Aalto, Finland
 e-mail: tuomas.k.savolainen@aalto.fi
[3] Aalto University Metsähovi Radio Observatory, Metsähovintie 114, 02540 Kylmälä, Finland
[4] Max-Planck-Institut für Radioastronomie, Auf dem Hügel 69, 53121 Bonn, Germany

## ABSTRACT

Rotations of the electric vector position angle (EVPA) in blazars are often close to an integral multiple of $180°$. There are many examples of this in the literature, and we strengthen the evidence by showing that, in the RoboPol monitoring program, $n\pi$ rotations occur more frequently than otherwise expected by chance. We explain this using a model consisting of two polarized emission components: a "jet" that is constant in time and a "burst" that is variable. The EVPA of the combination is $\text{EVPA}_{jet}$ at both the beginning and the end of the burst, so the net rotation across the burst must be $n\pi$. Several examples of this model are analyzed on the Stokes plane, where the winding number for the Stokes vector of the combination gives the value of $n$. The main conclusion is that the EVPA rotation can be much larger than the physical rotation of the emission region around the axis of the jet, but this requires the EVPAs of the jet and the burst to be nearly orthogonal. Shock-in-jet calculations can provide a physical model for our toy model and in addition they automatically give the required orthogonality. The model is illustrated with data from the literature on OJ 287. We suggest that the large rapid EVPA rotation seen in OJ 287 might be a phase effect and not representative of a physical rotation.

**Key words.** polarization – jets – galaxies: active – blazars: individual: OJ 287

## 1. Introduction

Blazars typically show strongly variable emission at radio through X-ray wavelengths and some emit $\gamma$-rays and high-energy particles. In this paper, our interest is focused on the polarization of this emission at radio, infrared, and optical wavelengths. The polarization is of particular interest because it contains information on the geometry, magnetic field structure, and physical mechanism of the source and because large rapid polarization changes sometimes appear to be associated with high-energy radiation.

The electric vector position angle (EVPA) can rotate substantially on a short time scale; that is, hours to days at optical to radio wavelengths, respectively, although typically the scale is much longer. The rotation can persist for a year or more and can be $360°$ and larger. The large rotations have been discussed as tracers of a moving emission region in a bent jet, or on a helical path, or in the disk (e.g., Kikuchi et al. 1988; Sillanpää et al. 1992; Marscher et al. 2008; Villforth et al. 2010; Myserlis et al. 2018). Linear models involving relativistic time-delay effects have also been discussed (Björnsson 1982; Zhang et al. 2014, 2015). Successive large rotations with a reversal in the sense of rotation have been seen (Cohen et al. 2018), with the reversal ascribed to magneto-hydrodynamic (MHD) effects.

D'Arcangelo et al. (2009) use three emission components to explain the behavior of OJ 287 at radio and near-IR wavelengths. The components are a narrow fast spine, a slow sheath, and the boundary region between the spine and the sheath. The variations in flux and polarization are due to transverse motions of the jet, which cause variations in the viewing angle.

Stochastic models have also been used to explain the large rotations (Jones et al. 1985; Jones 1988; Marscher 2014). In this class of models, the jet is turbulent and contains a large number of cells whose magnetic fields are oriented at random. At each time step the magnetic field in one cell is changed at random and the resulting random walk in the net EVPA can occasionally include large rotations. While many of the individual rotations can be explained with such a stochastic model, it has been shown that it is unlikely that all the observed rotations would be produced by a random walk mechanism (Blinov et al. 2015; Kiehlmann et al. 2016, 2017).

In this paper, we develop a two-component model consisting of a steady "jet" and a time-dependent "burst". The sum of these two can have a large variety of EVPA rotations, some of which are presented below. The general scheme of representing a polarization event as a sum of two components is an old idea (e.g., Björnsson 1982; Sillanpää et al. 1992; Villforth et al. 2010) and the model we use is essentially the same as the one used our earlier paper on OJ 287 (Cohen et al. 2018). However, in the present paper we emphasize that the EVPA rotation can be a phase effect and does not necessarily represent a physical rotation of an emission region. If the strengths of the two components become similar while the EVPAs are nearly perpendicular, then the linear polarization of the sum will have a minimum, while the EVPA of the sum rotates rapidly, up to nearly $180°$. There is observational evidence for this effect, in that it has often been noted that there is a polarization minimum at the time of the fastest EVPA rotation. (e.g., Sillanpää et al. 1993; Blinov et al. 2016a).

A two-component model is also useful if the variability is a function of frequency, in addition to time. Holmes et al. (1984) used two components with fixed EVPA and fractional polariza-

tion, and with variable flux density, to explain the spectral polarization behavior of OJ 287, including a temporary 80° change in EVPA as a function of frequency.

Two-component models have typically taken one component as being steady while the other one is variable, and the combination produces the observed changes (e.g., Cohen et al. 2018). The existence of a quasi-steady component can be justified with observations. Examples include a study of OJ 287 at R-band by Villforth et al. (2010) who noted that there was an "... underlying stable source of polarized emission" which they called the optical polarization core (OPC). Myserlis et al. (2018) similarly found a stable EVPA for OJ 287, at radio wavelengths. Pushkarev et al. (2017) showed, at radio wavelengths, that while AGN generally are variable, 40% of their sample showed a tendency for a preferred EVPA in the VLBI core over time, while Januzzi et al. (1994) and Hovatta et al. (2016) showed that many BL Lacs had a preferred polarization angle. However, there exists also a number of blazars that show almost continuous variability in their optical EVPA (Marscher et al. 2017).

In this paper, we present results on the Stokes (Q,U) plane, as loops generated by the rotating Stokes vectors. The topology of the loops, especially whether they do or do not enclose the origin of the (Q,U) plane, controls whether or not the EVPA will have a large rotation. The number of times a loop encloses the origin is called the index or winding number of the loop (Ahlfors 1979), and is positive if the rotation is counter-clockwise (CCW), negative otherwise. Villforth et al. (2010) have discussed the EVPA of OJ 287 at R-band in terms of these loops; see also Sasada et al. (2011) for 1510–089 and Larionov et al. (2016b) for CTA 102.

The plan for this paper is as follows. In Section 2, we review the observational evidence for EVPA rotations being preferentially on the order of $n\pi$, where $n$ is an integer and make this more precise by analyzing the Robopol data (Blinov et al. 2015, 2016a). The result is that in this data set, $n\pi$ rotations occur more often than otherwise expected by chance. In Section 3, we give a simple argument as to why an $n\pi$ rotation might be expected when a source produces a burst that adds to the steady emission from the jet.

In Section 4, we describe our two-component model with the aid of rotating vectors on the Stokes plane. Section 5 gives limits to the relative strength of the two components, and their angular difference, for a 180° rotation. Section 6 shows some special cases where the geometry is constrained, but the results are unexpected. In Section 7, we show with a simple model that weak fluctuations can generate 180° swings of the EVPA, provided the jet and the burst are nearly orthogonally polarized. Section 8 contains brief comments on two theoretical ideas that might provide some support for the two-component model.

The blazar OJ 287 is used in Section 9 to illustrate some of these ideas. Section 10 contains a discussion of the results, and a summary is in Section 11. Appendix A contains a derivation of the limiting conditions for a 180° rotation for the two-component model.

## 2. 180° rotations

EVPA rotations of the order of 180° or 360° have often been reported in the literature; for example for 0727–115 (Aller et al. 1981); OJ 287 (Kikuchi et al. 1988; Cohen et al. 2018); 0954+658 (Morozova et al. 2014); 3C 279 (Sasada et al. 2011; Kiehlmann et al. 2016); 1510–089 (Sasada et al. 2011; Beaklini et al. 2017); BL Lac (Aller et al. 1981; Sillanpää et al. 1993; Raiteri et al. 2013); and 3C 454.3 (Gupta et al. 2017), and there are further examples from the RoboPol collaboration (Blinov et

al. 2015, 2016a,b). The RoboPol group carried out a large program of optical polarization monitoring of a statistically well-defined sample of blazars, and one of their aims was to study the statistics of the EVPA rotation events. They reported that the distribution of EVPA rotations peaked near 180°, although the peak is quite broad. We now consider this further and show that 180° and 360° rotations occur more frequently in the RoboPol data than what is expected, if they come from a uniform distribution.

During the three years of monitoring, RoboPol detected 40 EVPA rotation events in 24 sources (Blinov et al. 2015, 2016a,b). Their definition of a "rotation" requires $> 90°$ change in EVPA consisting of at least four measurements with significant EVPA swings between them. The detailed definition is given in Blinov et al. (2015). From these 40 rotations, we have selected those for which there are at least two measurements before and after the rotation event that can be used to estimate the steady EVPA. However, there is variation in how steady the EVPA is outside of the rotation events. In order to remove cases in which no characterisc EVPA can be defined outside of the rotations, we further filtered the data based on the scatter of the measurements. If the EVPA before or after a rotation event has (circular) standard deviation that is larger than 0.4 times the (circular) standard deviation of a uniform distribution, we excluded that rotation from further analysis. The chosen threshold is arbitrary, but we note that the exact value does not significantly affect the results obtained here[1]. The above selections yield 19 rotations in 17 sources, which are listed in Table 1.

Using RoboPol data, we calculate the difference between the weighted mean EVPA before and after the rotation event, $\Delta\theta_{\rm net}$. If there is only one rotation for the given source, we include in $\Delta\theta_{\rm net}$ all data points except those that belong to the rotation according to the RoboPol criteria. If there is more than one rotation in the EVPA curve, we include in $\Delta\theta_{\rm net}$ only those "non-rotating" data points that bracket the given rotation. In the case of RBPLJ1555+1111, we also exclude the first six data points from the beginning of the measurement series, since their average EVPA clearly deviates from the average EVPA of the measurements closer to the rotation event. We calculate the variance of the weighted mean EVPA as

$$\sigma_{\rm mean}^2 = \frac{1}{\Sigma_i 1/\sigma_i'^2}, \tag{1}$$

where $\sigma_i'^2 = \chi_\nu^2 \sigma_i^2$. Here $\sigma_i$ is the measurement error of $i$th EVPA point and $\chi_\nu^2$ is the reduced chi-square for the weighted mean with $\nu$ degrees of freedom, i.e., we scale the EVPA errors so that $\chi_\nu^2 = 1$ for $\sigma_i'^2$ in order to correct for potential overdispersion. Finally, the error on $\Delta\theta_{\rm net}$ is $\sigma(\Delta\theta_{\rm net}) = \sqrt{\sigma_{\rm mean,1}^2 + \sigma_{\rm mean,2}^2}$, where $\sigma_{\rm mean,1}^2$ and $\sigma_{\rm mean,2}^2$ are the errors of the mean EVPA before and after the swing, respectively. $\Delta\theta_{\rm net}$ and $\sigma(\Delta\theta_{\rm net})$ are given in the columns 2 and 3 of Table 1.

In the fourth column of Table 1, we show $\lambda$, the minimum difference between $\Delta\theta_{\rm net}$ and $n \cdot 180°$ in units of $\sigma$. The fraction of rotations that have $\Delta\theta_{\rm net} = n \cdot 180°$ within $2\sigma$ is high – 11 out of 19 or 58% (these are marked with a bold font in Table 1). There are seven such rotations consistent with $n = 1$, two rotations consistent with $n = 2$ and two rotations consistent with $n = 0$. The average uncertainty of $\Delta\theta_{\rm net}$ is $\pm11.0°$, which means

---

**Table 1.** Fully sampled EVPA rotations from the RoboPol program

| Source | $\Delta\theta_{net}$ (deg) | $\sigma(\Delta\theta_{net})$ (deg) | $\lambda$ ($\sigma$) | $\Delta\theta_{max}$ (deg) | References |
|---|---|---|---|---|---|
| RBPLJ0045+2127 | **+188.8** | **15.1** | **0.6** | +200 | Blinov et al. (2016b) |
| RBPLJ0136+4751 | -216.7 | 8.3 | 4.4 | -114/-109[a] | Blinov et al. (2016b) |
| RBPLJ0721+7120 | **-180.3** | **7.7** | **0.1** | -208 | Blinov et al. (2015) |
| RBPLJ1512-0905 | **+177.1** | **21.3** | **0.1** | +242 | Blinov et al. (2016a) |
| RBPLJ1555+1111[b] | +138.6 | 7.1 | 5.8 | +145 | Blinov et al. (2016a) |
| RBPLJ1558+5625 | +139.9 | 15.9 | 2.5 | +222 | Blinov et al. (2015) |
| RBPLJ1635+3808 | **-4.7** | **15.8** | **0.3** | -119 | Blinov et al. (2016b) |
| RBPLJ1748+7005 | -207.5 | 12.4 | 2.2 | -127 | Blinov et al. (2016a) |
| RBPLJ1751+0939 | **-197.7** | **9.1** | **1.9** | -225 | Blinov et al. (2016b) |
| RBPLJ1800+7828 | **-166.6** | **11.9** | **1.1** | -192 | Blinov et al. (2016a) |
| RBPLJ1806+6949 | **-361.6** | **8.4** | **0.2** | -347 | Blinov et al. (2015) |
| RBPLJ1836+3136 | **+12.5** | **18.0** | **0.7** | +182 | Blinov et al. (2016b) |
| RBPLJ1927+6117 | -29.1 | 8.2 | 3.5 | -105 | Blinov et al. (2015) |
| RBPLJ2202+4216 | -153.7 | 9.9 | 2.7 | -253 | Blinov et al. (2015) |
| RBPLJ2232+1143 | **-364.6** | **11.3** | **0.4** | -312 | Blinov et al. (2015) |
| | **-170.5** | **5.8** | **1.6** | -140 | Blinov et al. (2015) |
| RBPLJ2243+2021 | **-168.8** | **9.3** | **1.2** | -183 | Blinov et al. (2015) |
| RBPLJ2253+1608 | -108.2 | 5.9 | 12.2 | -129 | Blinov et al. (2015) |
| | +121.3 | 7.8 | 7.5 | +145 | Blinov et al. (2016a) |

**Notes.** [a] The rotation is in two parts. [b] First six data points were excluded.

that we would on average expect $(2 \cdot 2 \cdot 11.0)/180 = 24\%$ of the cases to be consistent with $\Delta\theta_{net} = n \cdot 180°$ within $2\sigma$, if the $\Delta\theta_{net}$ were random and uniformly distributed. The observed fraction of $n\pi$ rotations is much higher than this. A simple Monte Carlo calculation gives a probability of $p = 0.002$ for having 11 or more rotations within $2\sigma$ of $n\pi$, out of 19 cases in total, if $\Delta\theta_{net}$ are randomly drawn from a uniform distribution between 0 and $n \cdot 180°(n \neq 0)$. The $\sigma$ used in the Monte Carlo rounds are bootstrapped from the observed values.

The original definition for RoboPol rotation events required an EVPA change of $> 90°$ (Blinov et al. 2015) and this may slightly bias our statistics. If only events with $|\Delta\theta_{net}| > 90°$ are considered, there are nine out of 16 rotations that are within $2\sigma$ of $n\pi$. In this case, a Monte Carlo simulation gives a probability of $p = 0.006$ for having nine or more $n\pi$ events, out of 16 in total, if they were drawn from a uniform distribution. Hence, we conclude that $\Delta\theta_{net}$ in the RoboPol data are unlikely to be uniformly distributed and that there seems to be overrepresentation of $n\pi$ rotations, which is consistent with the model we propose in Section 3.

Table 1 also shows $\Delta\theta_{max}$, the length of the continuous rotation determined in Blinov et al. (2015, 2016a,b). Of the 11 $n\pi$ rotations marked in boldface in Table 1, there are five cases in which $\Delta\theta_{max}$ significantly "overshoots" $\Delta\theta_{net}$. Such a behavior is seen in Figures 6c and 7c and can be explained by a multicomponent model or a model including internal noise-like variability in EVPA. In three cases out of 19, $|\Delta\theta_{max}|$ falls short of the total change in the average EVPA before and after the rotation event. This can be explained if part of the continuous rotation is missed due to a gap in the sampling. Another cause for too short measured $|\Delta\theta_{max}|$ values comes from the definition of the rotation used in RoboPol papers: the rotation is terminated when there is a change of sign in the EVPA swing. This means that $\Delta\theta_{max}$ will miss non-monotonic 180° rotation events such as the one shown in Figure 7c.

## 3. A simple argument for 180°

A simple argument shows that 180° rotations are expected in some circumstances. Consider the combination of a steady emission component and a temporary burst that rises from zero, goes through a maximum and then subsides back to zero. At the beginning and end of this event, the EVPA of the sum is $EVPA_{jet}$ and so the change in EVPA across the burst is 0°. This becomes non-trivial and interesting when we note that, for EVPA, 0° is the same as $n\pi$ where $n$ is an integer, and so the net EVPA swing must be $n\pi$. When the conditions are right, $n = 1$ and the rotation will be 180°. In the next sections, we describe a simple two-component model of this type, and find the limiting circumstances for a 180° rotation.

## 4. Two-component model

We use a simple model consisting of two components, a steady component that we call the "jet" and a variable component called the "burst". An example of the model is shown in Figure 1. This is the same as the model used in Cohen et al. (2018, see Figure 9), except that we now take the burst to have a parabolic amplitude. This burst is rather different from the typical radio outburst, which often has a sharp rise followed by a slower, approximately exponential, fall (e.g., Legg 1984; Valtaoja et al. 1999). But this shape applies to the total flux density, and we will be dealing exclusively with the polarized flux density, which we denote by PF, where P is the fractional linear polarization and F is the total flux density. Bursts in polarized flux can be highly irregular, because subcomponents can partially cancel one another, even when the total flux density is smooth. For simplicity, the burst has an EVPA that changes linearly with time. This too is hardly realistic, and observed EVPAs can be very irregular.

In Figure 1, the jet parameters are constant in time, with $PF_{jet} = 100$ and $EVPA_{jet} = 45°$. The burst has a parabolic shape with $PF_{burst,max} = 130$, an EVPA that increases linearly in time, and PF and EVPA are zero beyond $t = \pm w = \pm 10$. The important parameters are R, the flux ratio, R =
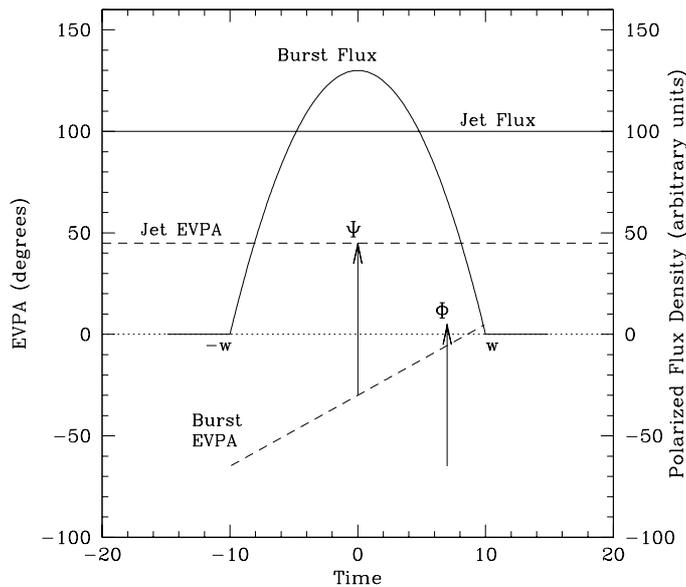
**Fig. 1.** Two-component model. Linearly polarized flux density is shown with solid lines, and EVPA is shown with dashed lines. Flux density and time are in arbitrary units. $\Phi$ is the EVPA rotation across the burst and $\Psi$ is the EVPA difference (jet – burst) at time $t = 0$. In this example, $\Phi = 70°$, $\Psi = 75°$, and R = ratio of peak burst flux to jet flux = 1.3.



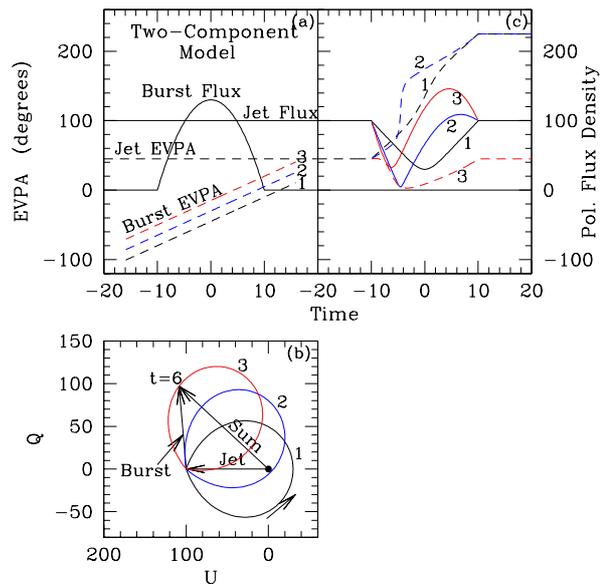**Fig. 2.** (a) As in Figure 1, but with three values of $\Psi$, $\Psi_1 = 90°$, $\Psi_2 = 75°$ and $\Psi_3 = 60°$. (b) Vectors on the Stokes (Q,U) plane. The jet vector is stationary. The 3 burst vectors rotate CCW around the tip of the jet vector, starting at $t = -10$ and ending at $t = +10$. The sum vector rotates around the origin. The arrow at bottom right shows the direction of time. The vectors for $\Psi_3$ are shown at $t = +6$. Loops 1 and 2 enclose the origin but loop 3 does not. (c) The polarized flux density, PF, and the EVPA, for the 3 cases in (b). Note that cases 1 and 2, which enclose the origin in (b), have EVPA rotations of 180°, while case 3 has a mild swing of 42.0° CW followed by a return to the starting level. Note also in (c) that case 2 has a deep PF minimum with a rapid EVPA swing, when the loop in (b) gets close to the origin.

$(PF_{burst,max}/PF_{jet})$; $\Phi$, the EVPA swing through the burst, $\Phi = (EVPA_{burst,w} - EVPA_{burst,-w})$; and $\Psi$, the EVPA difference at t=0, $\Psi = (EVPA_{jet} - EVPA_{burst,0})$. In Figure 1, R = 1.3, $\Phi = 70°$, and $\Psi = 75°$

The model in Figure 2a is the same as in Figure 1, but with three cases with different values of $\Psi$, $\Psi_1 = 90°$, $\Psi_2 = 75°$ and $\Psi_3 = 60°$. The parameter $\Psi$ is important for determining whether or not the EVPA can have a 180° rotation.

The Stokes vectors for the models in Figure 2a are plotted on the (Q,U) plane in Figure 2b. The vector for the jet is fixed with $Q_{jet} = 0$, $U_{jet} = 100$, and $\xi_{jet} = 90°$, where $\xi = \arctan(U/Q) = 2 \cdot EVPA$. The rotating vector for the burst is added to the jet vector to form the sum vector, which begins and ends its swing at the same place; namely, at the jet vector. Thus the sum vector makes a closed loop. The three loops have the same shape but their axes are rotated by $\Delta\xi = 2\Delta\Psi$.

Figure 2c shows the observable quantities, the time-dependent linearly polarized flux density and the EVPA. It is instructive to examine the individual cases. For cases 1 and 2 the loop encloses the origin and so the total swing of $\xi_{sum}$ is 360°, and the total EVPA swing is $\xi_{sum}/2 = 180°$. Loop 2 comes close to the origin of the Stokes plane, and at that time the sum vector becomes small and its EVPA swings rapidly through about 90°, as can be seen in Figure 2c. Loop 3 does not enclose the origin and from $t = -10$ to $t = -9.2$ it swings CCW, then it swings CW to $t = -3.3$, and then CCW to $t = +10$; the total EVPA excursion is 42.5° and the net EVPA rotation is 0°.

The fluxes in Figure 2c can similarly be understood from the loops in Figure 2b. Loop 1 is symmetric around the Q axis, and $PF_1$ is symmetric around $t = 0$, where it has a minimum. At that time, the Stokes vectors for the jet and the burst are oppositely directed; their EVPAs are perpendicular ($\Psi_1 = 90°$), and their cancellation is maximum. Loop 2 comes close to the origin of the (Q,U) plane, where the sum vector, i.e., the polarized flux

density, becomes very small. The sharp minimum in PF comes at the same time as the peak rotation rate in EVPA.

That the peak rotation rate comes at the same time as the minimum in PF (or P) is a general feature of two-component models, in which a loop on the (Q,U) plane comes close to the origin. There is observational evidence to support this feature. For example, Blinov et al. (2016a) state that, in blazars, the polarization fraction P often has a minimum when the EVPA is rotating most rapidly. Further examples are given in Sillanpää et al. (1993); Marscher et al. (2008); Abdo et al. (2010b); Cohen et al. (2018).

## 5. Limits for the 180° rotation

In Figure 2b, the nature of the EVPA curve (the winding number) changes when the loop moves across the origin as $\Psi$ changes. Similar effects are found as R and $\Phi$ vary. This is summarized in Figure 3, which shows the "critical line" where the winding number changes from 0 below the line, to 1 above it. The equation for this line is $R = 1/(1 - (2\delta/\Phi)^2)$ where $\delta = (\Psi - 90°)$; that is, $\delta$ is the departure from orthogonality of the EVPAs of the jet and the burst. The critical line is derived in the appendix.

Points on the critical line produce (Q,U) loops that touch the origin. Points above the line produce loops that enclose the origin and have an EVPA rotation of 180°. Points below the line produce loops that do not enclose the origin and have a net rotation of 0°.
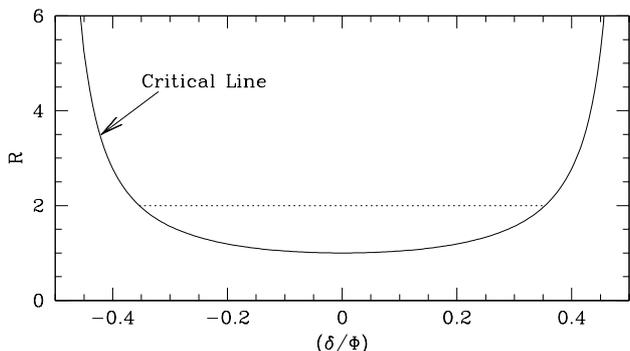
**Fig. 3.** Critical line for a 180° rotation, for the model in Figure 1. The quantities are defined in Figure 1, and $\delta \equiv (\Psi - 90°)$. The critical line is the locus of events $(R, \Phi, \delta)$ whose loops on the (Q,U) plane touch the origin. The dotted line shows the range of $(\delta/\Phi)$ for a 180° rotation, for R = 2. See text.

In Figure 3, the horizontal line at R = 2 shows the allowed range of $(\delta/\Phi)$ for a 180° rotation. If $\Phi$ is small, for example because the burst source is moving nearly along the axis of the jet, then there still is the possibility of a 180° rotation if $\delta$ is small enough. Thus, if R = 2, there will be a 180° rotation if $|\delta| < \Phi/(2\sqrt{2})$.

If the jet and burst are independent, then $\delta$ can be regarded as random, and for a fixed R and $\Phi$ the probability of a burst having a 180° rotation is proportional to the length of its horizontal line in Figure 3. For R = 2 and $\Phi = 10°$, $|\delta| < 3.5°$ for a 180° rotation, and if $\delta$ is random the probability for this is 7/180 = 0.04.

Figure 3 is valid only for our particular model, a parabolic burst with a linearly-changing phase, superimposed on a steady jet. Presumably, a similar but more realistic model would have an analogous line.

## 6. Special cases

From the preceeding discussion, we see that even as $\Phi$ becomes small, there remains a finite range of $\Psi$, centered on $\Psi = 90°$, where the model can have an EVPA rotation of 180°. Figure 4 shows the situation for $\Phi = 2°$ and two values for $\Psi$, 90° and 87°. The loops in Figure 4b are thin and the sum vectors sweep rapidly past the origin, twice, putting PF$_{sum}$ into the sharp minima seen in Figure 4c. In Figure 4c, the EVPA has two separated steps of about 90° each. For $\Psi = 90°$, the steps are both CCW and the total swing is 180°. But for $\Psi = 87°$, the loop does not enclose the origin and the EVPA steps are in the opposite sense, giving a net rotation of 0°.

It may seem rather remarkable that such a small physical rotation, 2° in this example, can lead to a 180° swing in the observed EVPA. We noted the possibility of such differences in our earlier paper on OJ 287 (Cohen et al. 2018), but without developing the general picture that we have here. The effect is a consequence of the circumstances discussed in Section 3. The EVPA across the burst changes by $n\pi$, and in Figure 4, $n = 0$ (red) and $n = 1$ (black). This requires a carefully chosen set of parameters, and in particular $\Psi$ must be close to 90°. As seen in Figure 3, the probability for this is small, if $\Psi$ is random. However, it seems unlikely that $\Psi$ is random, and $\Psi \sim 90°$ might not be rare in blazars.

Lyutikov et al. (2005) have shown that, for an unresolved optically thin jet with a helical magnetic field, the jet polariza-
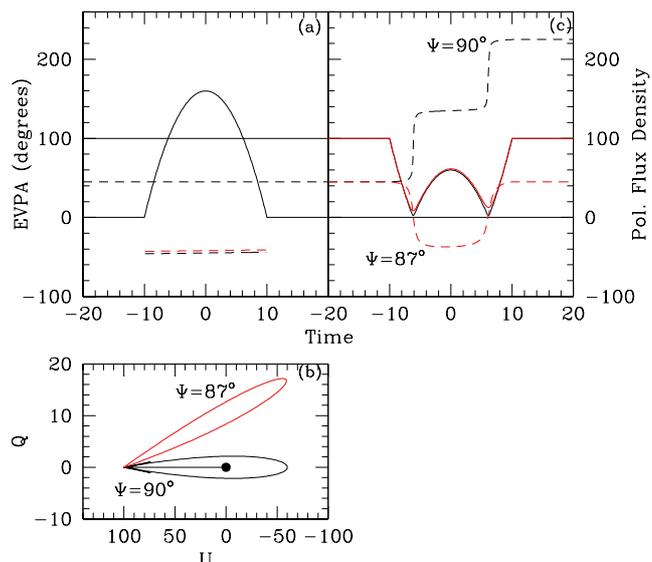


**Fig. 4.** Rotations with $\Phi = 2°$. Black: $\Psi = 90°$ and the loop in (b) encloses the origin. In (c), the two steps in EVPA are in the same direction and the net rotation is 180°. Red: $\Psi = 87°$ and the loop in (b) does not enclose the origin. In (c), the two steps are in opposite directions and the net rotation is 0°. Note that the Q and U scales are different in (b).
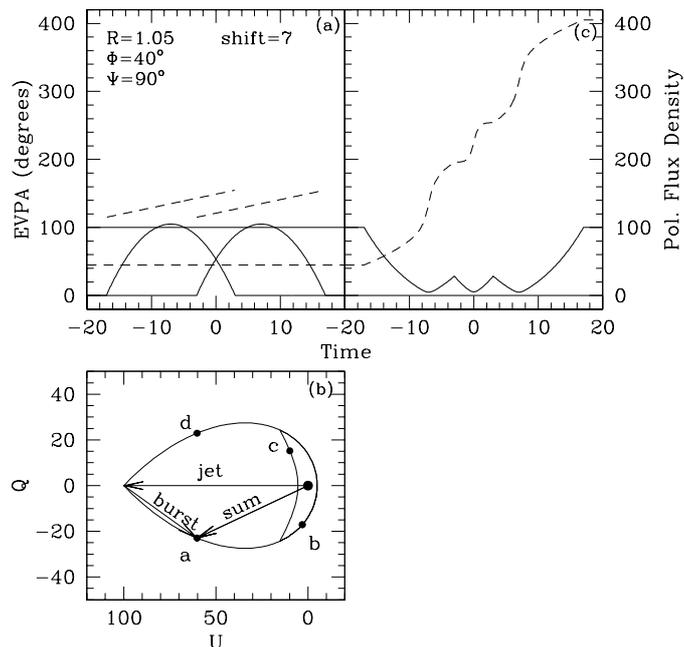


**Fig. 5.** Model containing two bursts. (a) As in Figure 2a but with two bursts shifted by $\Delta t = \pm 7$. (b) as in Figure 2b. The time sequence is a, b, c, b again, d. The loop encloses the origin twice, in the CCW direction, so the EVPA rotation in (c) is 360° CCW. See text.

tion should be either along or across the jet axis. Observational examples of this include Hodge et al. (2018), who showed for BL Lacs that the core polarization is preferentially along the jet. D'Arcangelo et al. (2009) showed that in 2005 at 43 GHz the polarization of an emerging new component in OJ 287 was

along the jet while the polarization of the background jet was perpendicular to the jet. See also Abdo et al. (2010a, Figure 8), where the blazar 1502+106 is seen at 15 GHz to have core EVPA roughly perpendicular to the jet in 2007, and parallel to the jet in 2008; and Aleksić et al. (2016, Figure 6) where IES 1011+496 similarly has core polarization roughly perpendicular to the jet in 2010, and along the jet in 2012. In both these last two cases, there were gamma-ray flares during the polarization rotation.

The double 90° step seen in Figure 4c is closely analogous to the similar double 90° step in the relativistic shock-in-jet calculation by Zhang et al. (2014, see Figures 7 and 17). In both cases, the second step comes when the disturbance relaxes and the system reverts to its original state. This is discussed further in Section 10. The value for $\Phi$ used in Figure 4, $\Phi = 2°$, is well below the fluctuation level seen in real situations, and so we expect that the topology of the loop, and the EVPA curve, could be strongly affected by fluctuations in the received signal. This is considered in Section 7.

Real bursts are generally not smooth like the parabola in Figure 1 and to simulate that we now allow the burst to have subcomponents. Figure 5 shows a case where the burst consists of two parabolas like that in Figure 1, with peaks at $t = \pm 7$. The EVPAs of the two subcomponents are similarly shifted. On the Stokes plane, Figure 5b, the sum vector rotates CCW, successively passing the points a, b, c, and b again, then d. It makes two complete loops around the origin, and the EVPA rotates by 360°, as shown in Figure 5c.
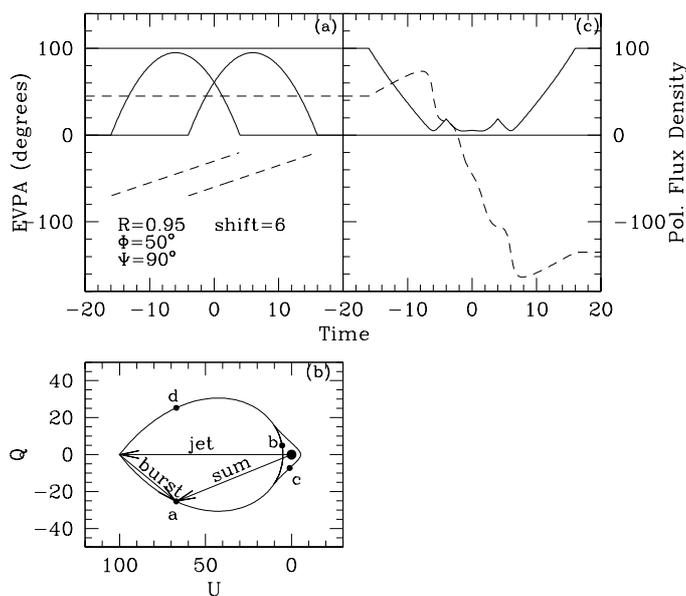


**Fig. 6.** (a) As in Figure 5 but with R = 0.95. (b) The time sequence is a, b, c, b again, d. The small loop encloses the origin once in the CW direction, and in (c) the net EVPA rotation is 180°, although the total swing is 237.4°. Note in (c) that the rotation is CW although in (a) the rotation of the bursts is CCW. Note also that the Q and U scales are different in (b).

The parameter R must be tightly tuned for the 2–loop situation seen in Figure 5, where R = 1.05. If R is reduced below 1.0 the topology changes, and the sum vector rotates around the small loop in the opposite direction. Figure 6 shows an example of this behavior. The subcomponents are as in Figure 5, but with R = 0.95. The sum vector successively passes the points a, b, c, and b again, then d, and the direction of rotation around the small
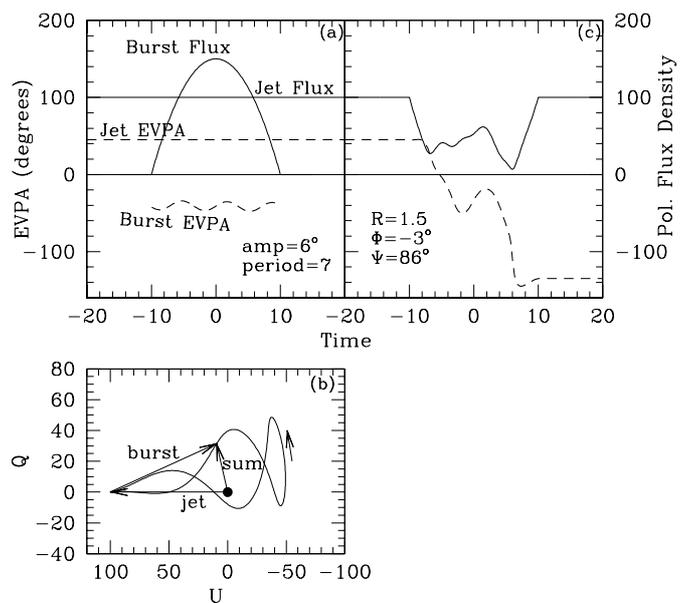
**Fig. 7.** Two–component model that simulates a burst with a fluctuating EVPA. (a) The burst EVPA has an overall slope of −3° and is modulated by a sine function with amplitude 6°. (b) The sum vector makes three loops on the (Q,U) plane, with the middle loop enclosing the origin. The jet, burst and sum vectors are shown at t = −6. The arrow shows the direction of time. In (c), the EVPA shows a non-monotonic CW swing of 180° plus a small overshoot. Note that the Q and U scales in (b) are different.

loop is CW. The total swing, shown in Figure 6c, is 237°, that is, larger than 180°, and the general rotation direction is CW, even though the rotation direction for the subcomponents is CCW.

The three cases shown in this section are special and require closely adjusted parameters. However, they do show that a simple interpretation of an observed EVPA rotation, for example in terms of a rotating emission region, might be wrong. The EVPA rotation can be a phase effect; it can be much larger than the physical rotation, and can even be in the opposite direction. Furthermore, a burst with a single sense of rotation can produce EVPA rotations in both senses, as in Figure 4c. This is particularly interesting because the observation of both rotation senses has been taken as an indication of a stochastic process (Kiehlmann et al. 2016), although here it results from a deterministic event. All these possibilities should be kept in mind when EVPA rotations are interpreted in terms of both physical and stochastic models.

## 7. Source fluctuations and measurement noise

In our model, the variable component changes smoothly, but in the real world the emission has rapid changes in PF and EVPA. As we now show, even small fluctuations can make large changes in the EVPA.

To simulate the effect of small fluctuations in the emission, we keep the two-component model with a steady jet, but allow the EVPA of the burst to have a sinusoidal ripple. This introduces 3 more parameters, the amplitude, period, and phase of the sine function, and the possibilities are thereby expanded. Figure 7 shows an example. In Figure 7, R = 1.5, $\Psi = 86°$ and the EVPA of the burst has a ripple of amplitude 6°, with an overall slope of $\Phi = -3°$. The motion of the sum vector defines 3 loops, with the central one enclosing the origin and generating a CW EVPA

rotation of 180°, as seen in Figure 7c. In this case, the topology in Figure 7b is set by the sine wave and the overall slope $\Phi$ could be changed from −3° to +3° with little effect. If R is increased, the pattern expands outward and when the origin is not in a loop there is not a 180° rotation across the burst. But when the expansion is continued, the innermost loop encloses the origin and again there is a 180° rotation, but in the CCW sense. In this case, the 180° would consist of two 90° CCW swings, near the beginning and end of the burst. If R is decreased below unity, there are no 180° rotations.

In some circumstances, measurement noise can also be responsible for large changes in EVPA. We consider an example of this with reference to Figure 2. In Figure 2b, the loop for case 2 comes close to the origin of the (Q,U) plane and at that time, the amplitude of the sum vector has a deep minimum. The measurement errors in Q and U are generally independent, and the actual track of the Stokes vector would be a jittery version of loop 2 in Figure 2b. A random small change in Q and/or U near the time of PF minimum could throw the loop across the origin, change the winding number, and so change the net EVPA rotation from 180° to 0°. The effect can be described with Figure 2c, where $EVPA_2$ has a ∼ 90° CCW swing at the time of minimum flux, and a net EVPA change of 180°. If noise were to throw the loop across the origin, then the EVPA curve would be similar except that the 90° swing at minimum flux would be in the CW direction and the net change would be 0°.

From these examples, it appears likely that small fluctuations in the signal, or small variations in Q and U due to noise, can cause large changes in the EVPA. These effects would appear when the loop is close to the origin of the (Q,U) plane; that is, when the amplitude is in a deep minimum.

## 8. Physical models

In this section, we first consider the shock-in-jet calculations by Zhang et al. (2014, 2015) and then the MHD calculations by Nakamura et al. (2010) and Nakamura & Meier (2014). These provide some theoretical support for our two-component model.

Zhang et al. (2014, 2015) calculate the radiation from a transverse shock in a relativistic cylindrical plasma jet in a helical magnetic field. For our purposes, it can be regarded as a two-component model, with the background jet being the first component, and the burst produced by the passage of the shock being the second component. Integration to find the radiation from the shock is in elementary diagonal disks that allow for the light-travel time across the jet, such that all photons from a disk are received at the same time by the observer. This means that a burst starts at zero amplitude, builds up to some peak amplitude that may persist for a while, and then symmetrically goes to zero. This is closely analogous to our parabola model. The parameters in the calculation can be picked to give the same results as we obtained; for example, the double 90° step in Zhang et al. (2014, Figure 7) is the same as the double 90° step in Figure 4 above.

The geometry of the system automatically makes the radiation from the jet and the burst orthogonally polarized, if the pitch angle of the helical field and the angle to the line-of-sight are in the appropriate ranges. This has been discussed in detail by Lyutikov et al. (2005). The shock-in-jet model of course is itself an idealized case, with perfect cylindrical symmetry, but it does provide a physical model for the two-component model as we have used it.

In our two-component model, the net EVPA rotation can be 180° if the EVPA rotation in the burst itself; that is, the quantity $\Phi$ in Figure 1, is small, provided the EVPA difference between

the jet and the burst is close to 90°. In a realistic situation, $\Phi$ can be small, but not zero; that is, the burst must have some rotation. Where does this rotation come from? One possible answer lies in the work of Nakamura (2001) and Nakamura et al. (2010), who studied a shock in a relativistic jet that is threaded by a helical magnetic field. They showed that the shock compresses the toroidal component of the field, and the resulting increase of angular momentum in the field is balanced by a counter-rotation in the plasma. The passage of the shock, with its rotating plasma, will produce a burst of emission with a rotating EVPA. This burst emission adds to the jet emission and, if the conditions are right, the observed net rotation can be 180°. In addition, if the jet speed is higher than the speed of the fast magnetosonic wave, then the reverse shock will be carried forward in the galaxy frame, and its radiation also will have an EVPA rotation, but in the opposite sense from that of the original forward shock (Nakamura & Meier 2014). This mechanism was suggested as a means for generating the rotations with reversals in successive bursts in OJ 287 (Cohen et al. 2018). In the next section, analyzing more recent data on OJ 287, the rotations are all CCW, and the simpler version, with the jet speed faster than the slow magnetosonic wave but slower than the fast magnetosonic wave, might be responsible for $\Phi$, the rotation in the burst.
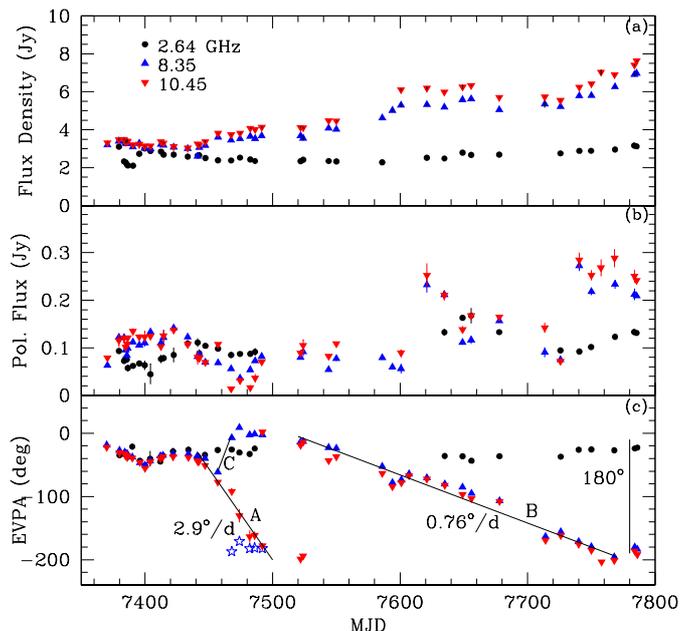
## 9. OJ 287

In this section, we illustrate the use of our model with high-cadence polarization observations of OJ 287 published by Myserlis et al. (2018). We obtained the relevant data from the CDS archive, and repeat part of it here in Figure 8; namely, Stokes I ($\equiv$ F) and EVPA at 2.64, 8.35, and 10.45 GHz (panels a and c), and the linearly polarized flux density PF (panel b). PF is found by multiplying F by $m_l$ ($\equiv$ P), the fractional linear polarization, which are in the CDS archive. Some of the epochs for I and $m_l$ are not identical, and we only used data for which the epochs differ by 0.2$d$ or less. Error bars for P, F, and EVPA are in the CDS archive, and the error bars for PF are found with standard propagation of errors. In all three panels of Figure 8, most of the error bars are smaller than the points.

The EVPA plot in Figure 8c differs from the Myserlis et al plot (their Figure 1c) in that we have introduced a +180° jump at 10.45 GHz, at MJD 7492, to make it easier to see that the 8.35 GHz and 10.45 GHz points are closely similar after that date. Three 10.45 GHz points near MJD7500 are duplicated with a separation of 180°, to help in following the change in slope, and we added a vertical bar of length 180° at MJD 7780, to emphasize that the EVPA is nearly the same at all three frequencies at the end of the data run. In addition we corrected all the EVPA values for Galactic Faraday rotation, using RM = +31.2 rad m$^{-2}$ (Taylor et al. 2009).

The short line at MJD 7460 connects points at 8.35 GHz that are 54° apart. This is the customary connection, whereby $n\pi$ is added to an EVPA value to make adjacent points differ by less than 90°. This is the connection that was used by Myserlis et al. (2018) and is seen in their Figure 1. With it we see that the behavior of the EVPA in the interval MJD 7440–7500 is different at 8.35 GHz and 10.45 GHz. At the higher frequency, there is a rotation of at least 140° CW, while at the lower frequency the rotation is about 70° CCW. This is surprising, since the frequencies are only 0.1 dex apart, and the spectrum is rather flat, with index $\alpha \sim 0.5$ (Myserlis et al. 2018).

An alternative connection for the 8.45 GHz points subtracts 180° at MJD 7472 and later, giving a jump of −126° CW. The first five of these points are shown with stars in Figure 8c. There

**Fig. 8.** Data from Myserlis et al. (2018) for OJ 287. (a) total flux density (Stokes I) (b) linearly polarized flux density (c) EVPA. The 180° step at MJD 7492 in (c), at 10.45 GHz, is introduced to show that the EVPAs at 8.35 and 10.45 GHz are closely similar after that date. The five stars are 180° below the corresponding 8.35 GHz triangles and are discussed in the text. Events A, B, and C are described in the text. MJD 7400 corresponds to 12 January 2016.
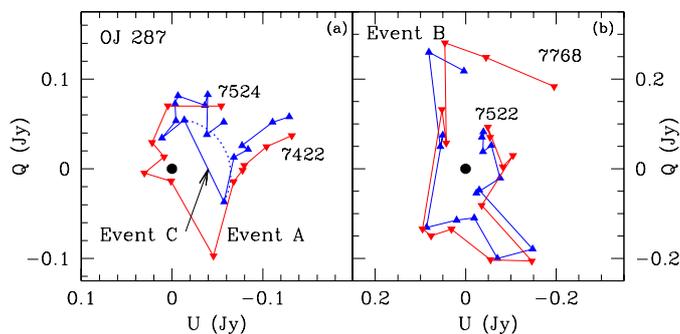


**Fig. 9.** Stokes plane showing the evolution of Q and U at 8.35 GHz (blue) and 10.45 GHz (red). (a) Events A and C, running from MJD 7422 to MJD 7524. Note that the 10.45 GHz loop (Event A) encloses the origin while the 8.35 GHz loop (Event C) does not. The dotted arc corresponds to the straight-line segments in Figures 8b and 8c; see text. (b) Event B, running from MJD 7522 to MJD 7768. Note that the scales in (a) and (b) are different.

still is a substantial difference between the curves at the two frequencies, since the 8.35 GHz curve now has an abrupt drop with a slope of at least $-4.9°/d$, while the 10.45 GHz curve has a steady drop of $-2.9°/d$. Hence, with either connection, we conclude that the EVPA curves show a substantial difference between 8.35 and 10.45 GHz. This is discussed further in Section 9.1. In the rest of this discussion, we use the first connection, consisting of the blue triangles in Figure 8c.

The two rotations seen at 10.45 GHz have different slopes as shown in Figure 8c, and we regard them as comprising two

distinct events, called A and B. Event B also appears in the 8.35 GHz data, and the polarized flux density and EVPA are closely similar at the two frequencies. The weak Event C appears at 8.35 GHz in the middle of Event A. These events are not seen at 2.64 GHz. Presumably, they occur deep in the core and are hidden by a large optical depth at 2.64 GHz.

The polarized flux densities in Figure 8b have deep minima at the time of Events A and C. This is not a coincidence but is a feature of our two-component model, described in Section 4, and is due to the (Q,U) loop coming close to the origin. Here we describe the details of these events.

In Event C, the 8.35 GHz points at first follow the 10.45 GHz points, then at MJD 7460 have a CCW rotation of about +75°. After the gap at MJD 7500, the 8.35 and 10.45 points lie close together and have a slow CW rotation of about 180°. The earlier rotation at 10.45 GHz follows a reverse S-shaped curve, with wings that slowly approach the base level, at least on the early side. The line marked $2.9°/d$ shows that the rotation is nearly uniform in its central region; this line is not a fit to the data but was drawn by eye.

The 10.45 GHz points at MJD 7492 and 7520 are duplicated with a separation of 180°, and probably belong to both events A and B. In our models (Section 4), the burst begins and ends at low amplitude, and so the net EVPA rotation must be gradual at the beginning and end of the event, as it is for Event A.

The slow rotation in Event B is the same at 8.35 and 10.45 GHz, and is not seen at 2.64 GHz. The line marked $0.76°/d$ is drawn by eye and shows that the rotation has small but significant departures from being uniform.

### 9.1. Stokes plane

The data in Figures 8b and 8c are shown on the Stokes plane in Figure 9. The fast EVPA rotation, defined somewhat arbitrarily in the interval MJD 7422 – MJD 7524, is in Figure 9a. We connected the successive (Q,U) points with straight lines, although these do not match the corresponding straight line segments in Figures 8b and 8c. In Figure 9a, the dotted arc corresponds to the straight segment C in Figure 8c, and its radius varies only a little because the corresponding PF endpoints are close together.

In Figure 9a, the loops at the two frequencies are similar, except that one encloses the origin and the other does not. Thus the two EVPA curves are different. This appears to be rather accidental, and perhaps due to fluctuations or simply to spectral differences in the polarized flux densities of the jet and the burst. If the amplitude of the 10.45 GHz burst had been 15% smaller, or the one at 8.35 GHz 20% larger, while the jet remained the same, then the two curves would have had the same rotation.

In Figure 9a, the loops are roughly symmetric about the line from the origin to the apex of the loop. This means that, in the two-component model, the jet and the burst must be nearly orthogonally polarized. This is the case for both Events A and C, at both frequencies.

In Figure 9b, the loop for Event B is essentially frequency-independent and is much slower that the fast loop in Figure 9a. Event B itself may be a multiple event with two major excursions in amplitude, seen at MJD 7620 and MJD 7740 in Figure 8b. Note that the scales in Figures 8a and 8b are different.

### 9.2. Two-component models

Figure 10a shows models for Events A and C in Figure 9a. Details of the models are in Table 2. The jet is the same for the two
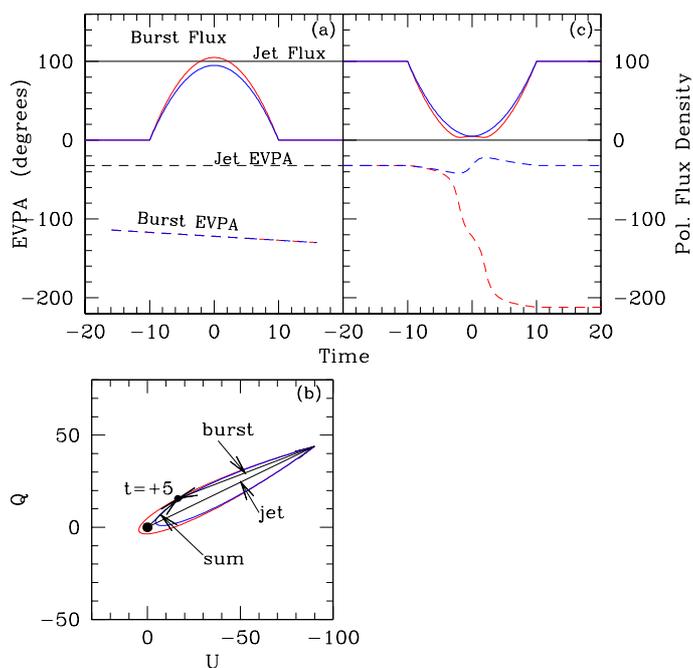
**Fig. 10.** Two-component models (Table 2) that have the same topology on the (Q,U) plane as the fast rotations in Figure 9a. The model for 8.35 GHz is blue, and that for 10.45 GHz is red. (a) as in Figure 1. (b) QU plane for the models in (a). The steady jet is shown as the long vector from the origin, the loops show the tracks of the sum (jet plus burst) vectors. The burst and sum vectors are shown at $t = +5$. (c) The flux density and EVPA of the sum. See text.

**Table 2.** Parameters for the models in Figure 10

| Frequency GHz | R | $\Phi$ (degr) | $\Psi$ (degr) |
|---|---|---|---|
| 8.35 | 0.95 | 10 | 90 |
| 10.45 | 1.05 | 10 | 90 |

frequencies and is constant in time. R is the ratio of the peak polarized flux of the parabola to that of the jet. The two ratios are roughly related by the spectral index of OJ 287, which is near 0.5. The angles $\Phi$ and $\Psi$ are shown in Figure 1; $\Phi$ is the total phase change across the burst, and $\Psi$ is the EVPA difference between the jet and the burst, at $t = 0$.

Figure 10b shows the models on the Stokes plane. Like the data (Figure 9), the 10.45 GHz loop (red) encloses the origin but the other one (blue) does not. However, they both come close to the origin on the (Q,U) plane and this makes the two model fluxes small at that time. In Figure 10c, showing the model observables, the EVPA is symmetric around $t = 0$, because we took $\Phi = 90°$. This symmetry can be seen in the data at 10.45 GHz, around MJD 7470. At 8.35 GHz the model EVPA (Figure 10c, blue) goes through an S-shaped excursion of amplitude 20°; the data go through a similar but larger excursion of 79° between MJD 7457 and MJD 7474. This is a large difference between the data and the model and this is discussed below.

The minima in the model amplitudes also match those in the data. In Figure 10c, at 10.35 GHz, the minimum consists of two low points with a slightly higher value in the middle. At 8.35 GHz there is a single minimum accurately located in the cen-

ter of the 10.45 GHz minimum. These both match the data in Figure 8b.

To produce all these similarities, the model parameters must be rather close to those in Table 2. We did not attempt to fit the models to the data, but did pick the parameters to bring the models close to some of the features in the data. Thus, the jet and the peak of the burst must be similar in amplitude and close to orthogonal, because the measured PF values are very low and time-symmetric. The value of $\Phi$ is not well-fixed. We chose $\Phi$, rather arbitrarily, as 10°, for both frequencies. This gives an 8-GHz S-shaped excursion around $t = 0$ with an amplitude of about 20°, while the data have a similar excursion of 79° between MJD 7457 and MJD.7474. Making $\Phi_{8.35}$ larger would increase the amplitude of the excursion and make the fit between the model and the data better; however, increasing $\Phi_{10.45}$ would change the nature of the flux minimum, turning the double dip into a single dip. We could choose different values of $\Phi$ at the two frequencies, but by the argument we used above they should be close together because the frequencies differ by only 0.1 dex.

This discrepancy in Event C at 8.35 GHz is the largest difference between the model results and the data. We suspect that it has to do with the poor match between the shape of the data loop in Figure 9a and the shape of the sum loop in the model, Figure 10. We used a parabola to simulate the amplitude of the burst, for simplicity. This gives a model that matches the data in several ways, but its smoothness is unlike that in real bursts, which usually are spiky and not symmetric around the peak. A better fit could no doubt be found by adding more parameters to the model. However, a detailed development of a model, together with a non-linear fitting procedure, does not seem warranted at this time.

Myserlis et al. (2018) regard the large EVPA rotations seen in Figure 8 as tracing motions of the emission region around a bend in the jet, or on a helical trajectory. We suggest, as an alternative, that they primarily are phase effects, as in the models in Figure 10. There are two reasons for this. First is the good fit of the data to the model, which has a physical rotation ($\Phi$) of only 10°. Admittedly, the value of $\Phi$ is not well fixed, but it appears to be much smaller than 180°.

A second reason to think that the model is correct and that the EVPA rotation is mainly a phase effect is the strong difference in the EVPA curves between 8.35 and 10.45 GHz. This difference is unlikely to be due to optical depth effects and is not readily explained in terms of helical or other motions. We ascribe it to a minor difference in the details of the bursts at the two frequencies. The burst and the jet are nearly orthogonal and have nearly equal values of PF, but the differences are enough to make the winding number at the two frequencies different. We suggest that the model does describe the real situation. It generates 180° rotations similar to those observed, and the required near-orthogonality is actually seen in the data (Myserlis et al. 2018).

## 10. Discussion

Our main result is the simple statement in Section 3, that the EVPA rotation across the combination of a burst with a steady jet is $n\pi$, where n is an integer. The first consequence of this is that small physical rotations of the source itself can lead to large EVPA rotations; for this to occur the background and the burst must have EVPAs that are close to orthogonal. The possibility of small physical rotations leading to large EVPA rotations was also noted in an earlier paper (Cohen et al. 2018).

The second consequence is that special behaviors are possible, especially in more realistic models where the the burst is not smooth. In Figure 5, the EVPA rotation is 360° CCW; and in Figure 6, using the same parameters except for a small change in the amplitude of the burst, the rotation is 180° CW plus a substantial overshoot. In the latter case, the EVPA rotation is in the opposite sense to the rotation of the sub-components. This drastic change comes about because the topology of the loop on the Stokes plane changes; the winding number changes from +2 to −1.

Another consequence is that small fluctuations can have large effects on the EVPA. In Figure 7, 6° fluctuations cause a rotation of 180°, and the rotation can be in either direction, depending on the relative amplitudes of the jet and the burst. In Section 9.2, we suggest that this process is responsible for the ∼ 180° EVPA rotation seen at 10.45 GHz but not at 8.35 GHz in OJ 287 (Myserlis et al. 2018). The fluctuations can also be due to internal noise and measurement error, which can change the winding number if PF is near a minimum. These are different processes from previous discussions of stochastic methods for generating large EVPA rotations, which use a set of randomly polarized emission cells (e.g., Kiehlmann et al. 2017). The large rotations occur in the random walk of the the net EVPA.

In our analyses, except for the sinusoidal ripple in Section 7, the burst has been smooth and its fall has been the reflection of its rise. But this is not realistic, and observed bursts in polarized flux are usually irregular in both EVPA and amplitude. This means that loops on the Stokes plane will be irregular, not smooth and symmetric as in Figures 2, 4, 5, and 6. We see this irregularity in Figure 9, which shows the Stokes plane for OJ 287. Other (Q,U) plots in the literature are similarly irregular; see for example Villforth et al. (2010, Figure 16) and Cohen et al. (2018, Figure 11).

The literature reports several cases where large EVPA rotations are closely similar at radio and optical or IR frequencies (e.g., Kikuchi et al. 1988; D'Arcangelo et al. 2009). and this has been taken as an indication that the source region is the same at both wavebands. In this case, the mechanism we have described might be at work, with the following scenario.

If the source region is the same for the two bands, then their geometries are similar. For the core of OJ 287 at 43 GHZ, D'Arcangelo et al. (2009) showed that the EVPAs of the background jet and the new component (presumably, a shock that generates the burst) were either parallel to or perpendicular to the position angle of the jet. This would apply at both wavebands and would give the opportunity for the jet and the burst to be orthogonal. The jet EVPA would be the same at both bands, and so the two rotations would start and end at the same EVPA. However, the details of the rotation would also be affected by the shape and amplitude of the bursts due to the shock, and further study is needed to establish if these could be similar at the two frequencies.

## 11. Summary and conclusions

We investigate a simple two-component model for generating large EVPA rotations in the emission from a blazar. The model consists of a steady "jet" and a variable "burst", although by "steady" we merely mean that this component has a much longer time constant than the more variable burst. These two components are represented by vectors on the Stokes (Q,U) plane, where the jet vector is fixed and the burst vector has variable amplitude and phase. The sum of the two vectors forms a loop on the (Q,U) plane, and is the observable quantity. The topology of the loop controls the EVPA swing, and the net EVPA rotation across the burst is $n\pi$ where $n$ is the winding number of the loop (number of times it encloses the origin.) Three parameters control the details of the rotation: R, the ratio of the peak polarized flux of the burst to that of the jet; $\Phi$, the overall EVPA swing of the burst; and $\Psi$, the EVPA difference between the jet and the burst at its peak. The allowed combinations of R, $\Phi$, and $\Psi$ for the net rotation of EVPA to be 180° rather than 0° are shown in Figure 3. The possibility for a 180° swing always exists for $R > 1$ provided the point is above the critical line in Figure 3, but if $\Phi$ is small then $\Psi$ must be close to 90°; that is, the EVPAs for the jet and burst must be nearly perpendicular. This means that a 180° swing can be generated with little EVPA rotation in the burst itself. This is a phase effect and does not require the physical rotation in the plasma to be comparable to that in the observed EVPA.

The model can accomodate a wide variety of behaviors, many of which are seen in the observations. If $\Phi$ is small, then the (Q,U) loop is thin, and the rotation can consist of two separated 90° swings, which can be of the same or opposite sense, giving a net rotation of 180° or 0° (see Figure 4). If the burst has structure as in Figure 5, then the EVPA swing is stepped and, since in this case the winding number is 2, the net swing across the burst is 360°. In Figure 6, the parameters are carefully chosen, but this example shows that the observed EVPA rotation can be in the opposite sense from that of the burst itself. In cases where the net swing is 180°, the EVPA can have an overshoot, as in Figure 6, where the overall swing is 237°. Small fluctuations in the burst, or system noise, can provide variations in R, $\Phi$ or $\Psi$ that cause 180° rotations. For this to occur R must be near unity and $\Psi$ must be near 90°.

The use of the model is illustrated with recent data from OJ 287 at 2.64, 8.35, and 10.45 GHz (Myserlis et al. 2018). At 10.45 GHz, there are two EVPA rotations of order 180°. Although they are adjacent in time, we regard them as different events because the rates are different, and because one of them appears only at 10.45 GHz. We suggest that the difference in the EVPA behavior between 8.35 GHz and 10.45 GHz is accidental, and is due to small differences in the bursts (or the jet) at the two frequencies such that the winding numbers are different. We briefly consider the observations of simultaneous EVPA rotations at radio and IR or optical bands, and show how our model provides a plausible mechanism for this phenomenon.

The shock-in-jet model of Zhang et al. (2014, 2015) has two emission components, the quiescent jet and the transverse shock. Integration across the shocked region that keeps track of the light-travel time gives a symmetric burst of emission, similar to our parabolic burst. Results for the EVPA rotation can be closely similar to our results in Section 4. The required orthogonality of the two components is not an ad-hoc assumption but is a result of the helical nature of the magnetic field and the symmetry of the system.

We conclude that the two-component model can explain a wide variety of observed EVPA rotations. Under certain conditions, the rotations can be phase effects, with little connection to physical rotations in the plasma.

# References

Abdo, A.A., Ackermann, M., Ajello, M., et al. 2010a, ApJ, 710, 810
Abdo, A.A., Ackermann, M., Ajello, M., et al. 2010b, Nature, 463, 919
Ahlfors, L. 1979, Complex Analysis (McGraw-Hill), 115
Aleksić, S., Ansoldi, S., Antonelli, L.A., et al. 2016, A&A, 591, A10
Aller, H.D., Hodge, P.E., & Aller, M.F. 1981, ApJ, 248, L5
Beaklini, P.P.B., Dominici, T.P., & Abraham, Z, 2017, A&A, 606, A87
Björnsson, C-I 1982, ApJ, 260, 855
Blinov, D., Pavlidou, V., Papadakis, I.E., et al. 2015, MNRAS, 453, 1669
Blinov, D., Pavlidou, V., Papadakis, I.E., et al. 2016a, MNRAS, 457, 2252
Blinov, D., Pavlidou, V., Papadakis, I.E., et al. 2016b, MNRAS, 462, 1775
Cohen, M.H. 2017, Galaxies, 5, 12
Cohen, M.H., Aller,H.D., Aller, M.F., et al. 2018, ApJ, 862, 1
D'Arcangelo F. D., Marscher, A.P,. Jorstad, S.G., et al. 2009, ApJ, 697, 985
Foschini, L., Ghisellini, G,, Kovalev, Y.Y., et al. 2011, MNRAS, 413, 1617
Gupta, A.C., Mangalam, A., Witta, P.J., et al. 2017, MNRAS, 472, 788
Hamaker, J. P. & Bregman, J. D. 1996, A&AS, 117, 161
Hodge, M.A., Lister, M.L., Aller, M.F., et al. 2018, ApJ, 862, 151
Holmes, P.A., Brand, W.J.L., & Impey, C.D., 1984, MNRAS, 211, 497
Hovatta, T., Lindfors, E., Blinov, V., et al. 2016, A&A, 596, A78
Januzzi, B.T., Smith, P.S., & Elston, R. 1994, ApJ, 428, 130
Jones, T.W., Rudnick, L., Aller, H.D., et al. 1985, ApJ, 290, 627
Jones, T.W. 1988, ApJ, 332, 678
Kiehlmann, S., Savolainen, T., Jorstad, S.G., et al. 2016, A&A, 590, 10
Kiehlmann, S., Blinov, D., Pearson, T.J., & Liodakis, I. 2017, MNRAS, 472, 3589
Kikuchi, S., Inoue, M., Mikami, Y., et al., 1988, A&A, 190, L8
Larionov, V. M., Jorstad, S.G., Marscher, A.P., et al. 2013, ApJ, 768, 40
Larionov, V. M., Villata, M., Raiteri, C.M., et al. 2016b, MNRAS, 461, 3047
Legg, T.H. 1984, in VLBI and Compact Radio Sources, eds. C. Fanti, K.I. Kellermann, & G. Setti (Dordrecht : Reidel), 183
Lyutikov, M., Pariev, V.I. & Gabuzda, D.C., 2005, MNRAS, 360, 869
Marscher, A.P., Jorstad, S.G., D'Arcangelo, F.D., et al. 2008, Nature, 452, 966
Marscher, A.P., Jorstad, S.G., Larionov, V.M., et al., 2010, ApJ, 710, L126
Marscher, A.P. 2014, ApJ, 780, 87
Marscher, A.P., Jorstad, S.G., & Williamson, K.E. 2017, Galaxies, 5, 63
Morozova, D.A., Larionov, V.M., Troitsky, I.S., et al. 2014, AJ, 148, 42
Myserlis, I., Komossa, S., Angelakis, E., et al., 2018, A&A, 619, A88
Nakamura, M., Ph.D. thesis, Formation of the Wiggled Structure of Radio Jets from Active Galactic Nuclei, 2001, Tokyo University of Science
Nakamura, M., Garofalo, D., & Meier, D. L. 2010, ApJ, 721, 1783
Nakamura, M., & Meier, D. L. 2014, ApJ, 785, 152
Pavlidou, V., Angelakis, E., Myserlis, I., et al. 2014, MNRAS, 442, 1693
Pushkarev, A.B., Kovalev, Y.Y., Aller, M.F., et al. 2017, Galaxies, 5, 93
Raiteri, C.M., Villata, M., D'Ammando, F., et al. 2013, MNRAS, 436, 1530
Sasada, M., Uemura, M., Fukazawa, Y., et al. 2011, PASJ, 63, 489
Sillanpää, A., Takalo, L.O., Nilsson, K., et al. 1992, A&A, 254, L33
Sillanpää, A., Takalo, L.O., Nilsson, K., & Kikuchi, S. 1993, Ap&SS, 206, 55
Taylor, A.R., Stil, J.M., & Sunstrum, C. 2009, ApJ, 702, 1230
Valtaoja, E., Lähteenmäki, A., Teräsranta, H., & Lainela, M. 1999, ApJS, 120, 95
Villforth, C., Nilsson, K., Heidt, J., et al. 2010, MNRAS, 402, 2087
Zhang, H., Chen, X., & Böttcher, M., 2014, ApJ, 789, 66
Zhang, H., Chen, X., & Böttcher, M., et al. 2015, ApJ, 804, 58

## Appendix A: Loops on the Stokes plane

Loop 2 in Figure 2b comes close to the origin of the (Q,U) plane, and the character of the associated EVPA curve changes if the axis of the loop rotates enough to change the winding number. Here we calculate the conditions for the loop to touch the origin.

We first find the time, $t_c$, at which the loop touches the origin. The Stokes parameters are additive and so we write $Q_{sum} = Q_{jet} + Q_{burst}$ and $U_{sum} = U_{jet} + U_{burst}$. When the loop touches the origin, $Q_{sum} = 0$ and $U_{sum} = 0$, or,

$$A\cos(\xi_{jet}) = -AR[1 - (t_c/w)^2]\cos(\xi_{jet} - 2\Psi + \Phi(t_c/w)), \quad \text{(A.1)}$$

$$A\sin(\xi_{jet}) = -AR[1 - (t_c/w)^2]\sin(\xi_{jet} - 2\Psi + \Phi(t_c/w)), \quad \text{(A.2)}$$

where A is the flux density of the jet, AR is the peak flux density of the burst, and $\Psi$ and $\Phi$ are defined in Figure 1. Squaring and adding gives $R^2[1 - (t_c/w)^2]^2 = 1$, and:

$$t_c = \pm w\sqrt{1 - 1/R}. \quad \text{(A.3)}$$

We choose the minus sign in the square root because $(t_c/w) \leq 1$.

At $t = t_c$ we can write:

$$EVPA_{burst,c} = EVPA_{jet} - \Psi + \Phi(t_c/2w) \quad \text{(A.4)}$$

$$= EVPA_{jet} - \Psi \pm (1/2)\Phi\sqrt{1 - 1/R}. \quad \text{(A.5)}$$

But at $t = t_c$, on the (Q,U) plane, the burst and jet vectors are opposite and cancel; hence $EVPA_{burst,c} = EVPA_{jet} \pm 90°$ and

$$\delta = \pm(1/2)\Phi\sqrt{1 - 1/R}, \quad \text{(A.6)}$$

where $\delta = (\Psi - 90°)$, or

$$R = [1 - (2\delta/\Phi)^2]^{-1}. \quad \text{(A.7)}$$

Equation (A.7) is plotted in Figure 3 as the critical line. Points on the line have (Q, U) loops that touch the origin. Points above the line have an EVPA rotation of 180°, while those below the line have a net rotation of 0°.